J Mater Sci (2024) 59:1087–1103

Metals & corrosion

Oxide scale microstructure and failure mechanism of alloy 601 under varying metal dusting conditions

C. Schlereth[1,*], M. Weiser[2], E. White[1], P. Felfer[2], and M. Galetz[1]

[1] *DECHEMA-Forschungsinstitut, Frankfurt am Main, Germany*
[2] *FAU Erlangen-Nürnberg, Erlangen, Germany*

Received: 21 July 2023
Accepted: 9 December 2023
Published online: 8 January 2024

ABSTRACT

Chemical plants which process highly carbonaceous gases at elevated temperatures are prone to catastrophic corrosion by metal dusting. Typically, commercial alloys with high amounts of protective oxide scale formers (Cr, Al, and Si) are used in these environments. However, scale failure is still frequently observed after an incubation time initiating pits. In this study, the microstructure and subsequent metal dusting-induced failure of the oxide scale on the commercial Ni-based alloy 601 was analyzed. Samples were exposed in different aggressive metal dusting gases and characterized using metallographic cross sections, electron beam microanalysis (EPMA), scanning electron microscopy (SEM), X-ray photoelectron spectroscopy (XPS), Raman spectroscopy and transmission electron microscopy (TEM). A thin and protective chromia scale formed in some regions with a continuous silica layer below. Across most of the alloy 601 surfaces, internal oxidation of Al could be linked to metallic particles in the outer scale. Additionally, $MnCr_2O_4$ was observed in the outer scale. Together with pores in the chromia, the spinel and metallic particles in the outer scale combined to provide pathways for carbon ingress. After exposure in a gas with a higher driving force for carbon deposition, a higher amount of carbon was incorporated in the growing oxide scale, resulting in earlier scale failure and metal dusting pit initiation.

Handling Editor: P. Nash.

Address correspondence to E-mail: clara.schlereth@dechema.de

https://doi.org/10.1007/s10853-023-09260-2

GRAPHICAL ABSTRACT

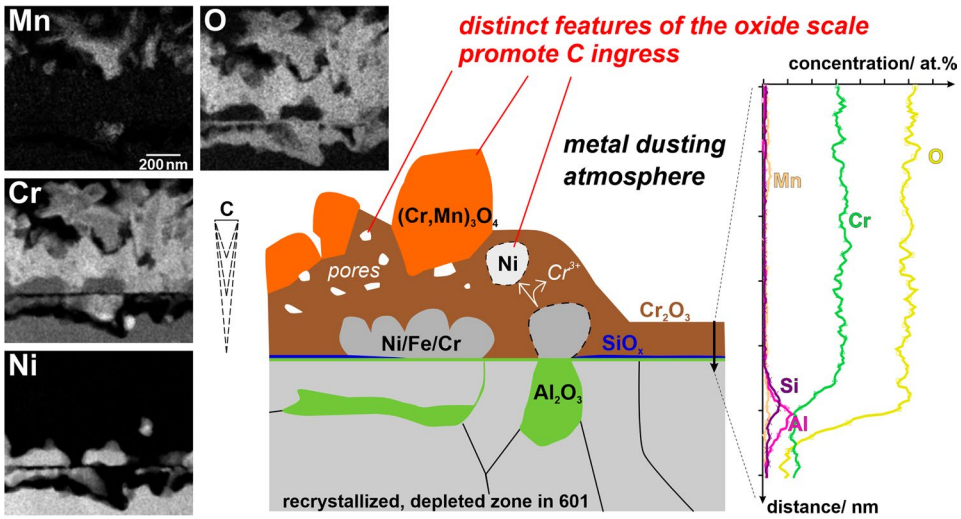

Introduction

The chemical industry is currently trending toward promoting carbon capture and storage, as well as fossil fuel-free routes for synthesis gas production, leading to more processes with a high risk for metal dusting. Corrosion by metal dusting is observed in processes with carbon-rich gases at temperatures of 400–800 °C [1, 2]. Ni, Fe, and Co catalyze deposition of solid carbon from the carbon-rich gas and the nucleation of graphite in the metallic matrix. The metal disintegrates from the graphite volume expansion leading to pit and coke formation. The coke contains amorphous carbon and graphite, as well as metal, oxide, and carbide particles [3–5].

Commercially Ni-based alloys are commonly used in high metal dusting risk environments. To establish and maintain a protective oxide scale, which acts as a barrier between the gas and the metal, Ni is alloyed with high amounts of Cr, along with Al and/or Si. However, the oxide scales can still fail and the pitting attack will continue unless major changes are made in the process gas [6]. Of course, maximum efficiency is targeted in all processes for economic and environmental improvement. This includes structural materials with high metal dusting resistance to minimize process changes, maintenance and plant downtime. Understanding and impeding scale failure and pit initiation under metal dusting conditions is a major step toward developing and selecting better materials for these applications.

The proposed protective barrier effect from chromia, alumina and/or silica scales clearly requires further investigation as to the mechanism of metal dusting initiation. The four most prominent hypotheses for pit formation through an oxide scale are briefly summarized in the following.

Cracks: gas transport through the oxide Mechanical failure of the oxide scale allows contact between the process gas and the depletion zone beneath the scale [1]. Pits will form when the oxide former concentration at the oxide/gas interface is insufficient to restore a protective scale.

Spinels: enhanced CO dissociation and/or carbon diffusion Several studies report an earlier failure of scales containing Fe-, Ni- or Mn-rich spinels when compared to pure chromia [7, 8]. The reactivity of the spinel with the carbon-rich gas can be explained with a dissociative adsorption mechanism of CO on Fe- and Mn-rich spinels [9], based on a similar mechanism of CO_2 on Fe-Ni-spinels [10–12]. A higher carbon deposition on $NiCr_2O_4$ was observed when compared to $FeCr_2O_4$ [13]. Also a higher or lower carbon deposition on Mn-Cr-spinels when compared to chromia was observed depending on the composition [14, 15]. The higher carbon solubility of Mn-Cr spinels as compared to chromia contributes to the less favorable performance [9].

Metallic Ni-rich particles: enhanced carbon diffusion Zeng, Natesan and co-workers [6, 16] suggested formation of metallic particles by the reduction of Ni-rich spinels within the oxide scale, thus providing a path for inward carbon diffusion.

Carbon enrichment along grain boundaries: enhanced carbon diffusion Enrichment of carbon along the oxide grain boundaries may also contribute to inward carbon diffusion. As the scales grow in a carbon-rich environment, carbon is partially incorporated directly during the oxide scale growth. It was shown that Cr_2O_3 and $Cr_{23}C_6$ can form simultaneously during reaction of CO with Cr at 830 °C [17]. Studies using atom probe tomography [18], transmission electron microscopy (TEM) [19], and Raman spectroscopy [20] report carbon enrichment along chromia grain boundaries and the presence of graphite within the chromia grains [9]. Interestingly, no graphite was found in the inner alumina layer [19].

In this study the microstructure of the oxide scale formed on the commercial Ni-based alloy 601 was analyzed, with a focus on the oxide scale failure mechanism under metal dusting conditions. The alloy was exposed in four gas mixtures with varying aggressivity (as discussed in [21]) with the goal of examining the influence of the gas composition on the oxide scale microstructure.

Experimental

A hot-rolled and solution-annealed plate of alloy 601 (2.4851, N06601) was provided by VDM Metals International GmbH. The composition is listed in Table 1. Samples were wire-cut to 20 by 10 mm from a 5 mm thick plate, with a hole drilled in one side for hanging in the exposure crucibles.

All sides of the samples were ground with SiC paper to a surface finish of P1200 grit, then sonicated in ethanol and finally rinsed with isopropanol. The samples were ground because in a comparison of industrially relevant surface treatments, ground samples showed the highest metal dusting resistance [22–24]. Sample masses were determined with a precision weighing balance (Mettler Toledo, 0.01 mg) and dimensions were taken with an electronic caliper. Two samples were prepared for each test condition.

The samples were suspended in separate slitted alumina crucibles and positioned in a horizontal tube furnace equipped for high pressure tests. A detailed description of the setup is given in [25]. The pressure vessel was made of a chromia forming Ni-based alloy (Centralloy ET45 Micro or Haynes 235). After the samples were placed in the pressure vessel, the tube was purged with Ar (< 2 vol. ppm O_2 impurities) overnight. The samples were heated to 620 °C in stagnant Ar. When the target temperature was reached, the test gas was introduced, and the total pressure was increased to 18 bar. Four test series with the gas compositions given in Table 2 were performed. During the tests, the gas flow was set to 0.02 cm/s at the samples.

It is common to calculate parameters based on the gas conditions in order to estimate the propensity of the gases to cause metal dusting. These parameters are all tools to estimate the driving force for carbon deposition at the surface. The driving force for carbon deposition is thought to correlate directly with the observed aggressivity of the attack. Hence, it is important to know the most suitable parameter to estimate the driving force for carbon deposition. For all of the gas compositions used in this study, the carbon activity $a_{C,syn}$ in the CO reduction, also called the synthesis gas reaction, was kept constant. The same applies for the $a_{C,Boud}$ for the Boudouard reaction. With this test matrix, the impact of the gas composition independent of these two parameters was studied. However, as reported in [21], no correlation was found between $a_{C,syn}$ or $a_{C,Boud}$ and the observed aggressivity. Instead, the propensity for the gases to cause metal dusting attack increases from I to IV based on the results from 601 and other alloys [21].

Table 1 Composition of alloy 601 in at.% and wt.% as determined by atomic emission spectroscopy (AES)

	Ni	Fe	Cr	Al	Si	Mo	C	Mn	Ti	Mg, V, W, Co, Zr, Cu, Nb
at.%	54.9	14.7	25.6	2.5	0.7	0.1	0.3	0.6	0.5	< 0.09
wt.%	58.2	14.8	24.0	1.2	0.3	0.1	0.1	0.6	0.5	0.005–0.09

Reproduced with permission from reference [21]. Copyright 2022, Elsevier B.V

Table 2 Gas compositions of the four test series, carbon activities and p_{O2} as calculated via FactSage 6.1, and the maximum exposure time for the alloy 601 samples

Gas	Component/vol.%					Carbon activity			$p_{O2\ metast}$/bar	Max. exposure time/h
	CO	CO_2	H_2	H_2O	Ar	$a_{C,syn}$	$a_{C,Boud}$	$a_{C,metast}$		
I	10	2	80	2	6	206	62	0.08	8.6×10^{-25}	960
II	10	2	40	1	47	206	62	0.76	4.0×10^{-24}	960
III	20	8	20	1	51	206	62	6.25	1.8×10^{-23}	980
IV	40	32	10	1	17	206	62	33.98	7.5×10^{-23}	480

Reproduced with permission from reference [21]. Copyright 2022, Elsevier B.V

A reasonable correlation between the aggressivity of the gas and the respective carbon activity in metastable thermodynamic equilibrium ($a_{C,metast}$), with suppression of graphite formation, was demonstrated using FactSage 6.1 [26]. For this parameter, the metastable thermodynamic equilibrium of the system is calculated using the CALPHAD approach. To obtain a measure for the driving force of carbon deposition in the system, the formation of graphite as the main solid carbon component is suppressed in the calculation. The resulting activity of graphite is given in $a_{C,metast}$. In contrast to $a_{C,syn}$ and $a_{C,Boud}$, all reactive species in the system are considered in the calculation of $a_{C,metast}$. Details of the carbon activity and estimated oxygen partial pressure ($p_{O2,metast}$) calculations were described in [21].

The quasi-isothermal exposure experiments were stopped every 240 or 260 h by releasing the pressure and cooling down the furnace simultaneously. The furnace was purged with Ar before the samples were removed. The accumulated coke was cleaned from the samples by an ultrasonic ethanol bath and rinsing with isopropanol. Subsequently, the specimens weighed and then reinserted into the furnace. Generally, four exposure segments were performed in each gas; however, in the most aggressive gas IV, massive coke formation occurred and thus the test was terminated after only two exposures which totaled 480 h.

After the final exposures, samples from each gas were cut for analysis, with one section galvanically plated with Ni for metallographic preparation. The Ni-plated cross sections were prepared for analysis of the oxide scale and cross sections without Ni plating were used for subsequent etching. All cross sections were ground with SiC paper down to P1200 grit and finally polished down to a 1 µm surface finish (using a diamond suspension). Electrolytic etching was applied with 10% oxalic acid. Element distribution maps were obtained with electron probe microanalysis (EPMA, JEOL JXA-8100). For electron backscatter diffraction (EBSD, EDAX velocity), a cross section was further prepared using OPU and milling with an ion beam (Hitachi IM4000).

The morphologies and compositions of the oxide scales were characterized using a scanning electron microscope (SEM, Hitachi SU 5000) and a transmission electron microscope (TEM, FEI Titan Themis^3 300). For the latter, lamellae were prepared from samples exposed in gas II and IV. The regions of interest were first protected with a Pt layer using a focused ion beam instrument (FIB, FEI Helios NanoLab 600i SEM). The selected lamellae were mounted on Cu lift-out grids. For thinning with a Ga^+ ion beam, the accelerating voltage was set to 30 kV and (beam) currents were reduced successively from 3 nA to 80 pA. Finally, a Ga^+ ion cleaning procedure at a reduced accelerating voltage (2 kV and 78 pA) was conducted to remove the remaining FIB damage. TEM micrographs were acquired with a high-angle annular dark field (HAADF) detector using Velox Thermofisher Software. To avoid overlaps, energy-dispersive X-ray spectroscopy (EDS) of the Kα-lines were preferentially used for the element maps and quantitative point analysis in scanning transmission electron microscopy (STEM-EDX) mode.

Surface depth profiles through the oxide scales were obtained with X-ray photoelectron spectroscopy (XPS, PHI Quantera II) and Ar ion sputtering (with 720 nm/min on SiO_2). Monochromatic Al-Kα radiation with a beam diameter of 200 µm and a pass energy of 26 eV was used. Quantification was based on the signals Cr 2p, Fe $2p_{1/2}$, Ni $2p_{3/2}$, Al 2s, Mn $2p_{3/2}$, Ti 2p, Si 2s, C 1s and O 1s.

Raman-spectroscopy (Renishaw inVia Raman Microscope) lasers with 532 nm and 633 nm wavelengths and a maximum power of 2 and 0.2 mW, respectively, were used to characterize the surface oxides. The obtained Raman spectra were analyzed with Spectragryph [27].

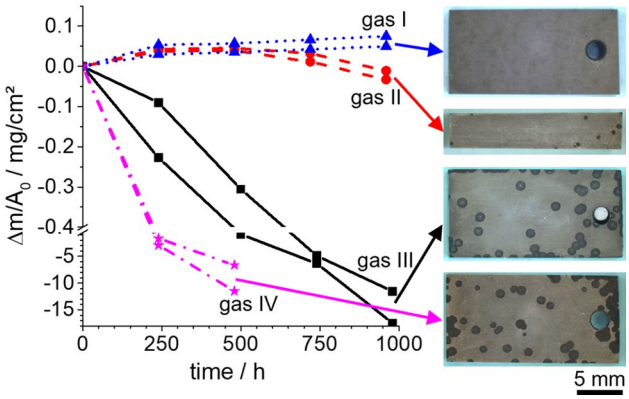

Figure 1 Specific mass loss of alloy 601 samples after exposure at 620 °C and 18 bar in gases I to IV. Light microscope images show samples after the last exposure (960 h for gases I and II, 980 h for gas III and 480 h for gas IV). For the samples exposed in gas II, the metal dusting pits formed only at the side surfaces, thus the side image is included only for gas II. Adapted with permission from reference [21]. Copyright 2022, Elsevier B.V

Results

The specific mass changes and representative macroscopic images of the samples after the final exposures are given in Fig. 1.

The most rapid mass loss was observed in gas IV, where the samples showed massive coke formation after only 480 h exposure. A similarly strong attack after 980 h was observed in gas III. In gas II, a few pits formed, but only on the side surfaces of the sample. These were manually ground and thus have a slightly different state of surface deformation than the machine ground main surfaces. No attack was observed on samples exposed in gas I after 960 h.

The etched light micrographs of the near-surface zones of the samples after final exposure are displayed in Fig. 2. The light microscope images of the etched cross sections all show a bright layer or "white ribbon" below the oxide scale.

The EBSD map in Fig. 3b, of a comparable area at a significantly higher resolution, confirms these "white ribbons" are recrystallized zones below the oxide scale. Figure 3a shows element maps of the sample exposed in gas II, these are representative for all 601 samples after the last exposure in the gases I to IV.

According to the element distribution maps, the thin oxide scale on the samples is rich in Cr, Al and Mn and the specimens were depleted in these elements below the oxide scales, accordingly. EPMA point measurements indicated that the Cr contents in the depleted zone were between 15 and 19 at.%, while the bulk content was 26 at.% Cr.

Figure 4 displays representative BSE images of the same oxide scales as in Fig. 3 for the different gases. The outer oxide scales exhibited irregular morphologies and the thicknesses varied widely between 70 and 800 nm. Pores (dark) and metallic (bright) particles were visible in the thicker regions of the oxide scales. Most of the metallic particles were directly adjacent to the initial metal surface, but some were distributed further above the original sample surface in the oxide. Internal oxidation was observed (darker regions below the original surfaces, which are indicated by dotted white lines) in all investigated cross sections.

To analyze the individual distribution of elements in the oxide scales and adjacent alloy regions for every metal dusting atmosphere, XPS depth profiles were measured (Fig. 5).

Ar ion sputtering depth depends on the elemental composition of the respective oxide phases and varies widely over the oxide scales due to their complexity. Combined with the uneven sample surfaces and the sputtering beam being inclined to 45°, all of displayed depth profiles are relatively flat and exhibit considerable elemental overlaps.

The XPS measurements show formation of an outer Cr-rich and inner Al-rich oxide. In addition, 1.0–1.6 at.% Ti was detected in the outer part of the

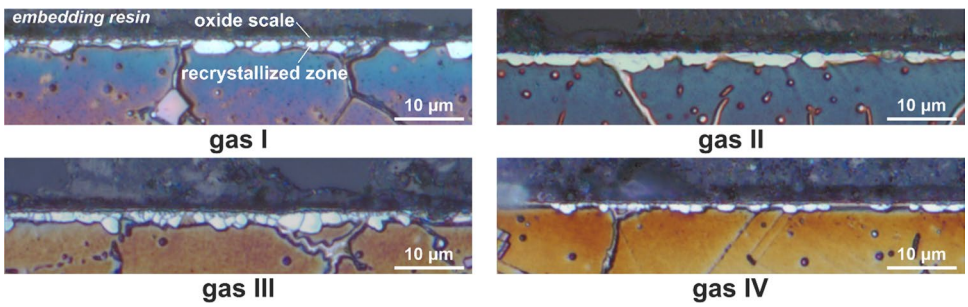

Figure 2 Top row: light microscope (LOM) images of etched cross sections of alloy 601 surface regions after exposure in gas I (960 h), gas II (960 h), gas III (980 h) and gas IV (480 h) at 620 °C and 18 bar. Adapted from [28]

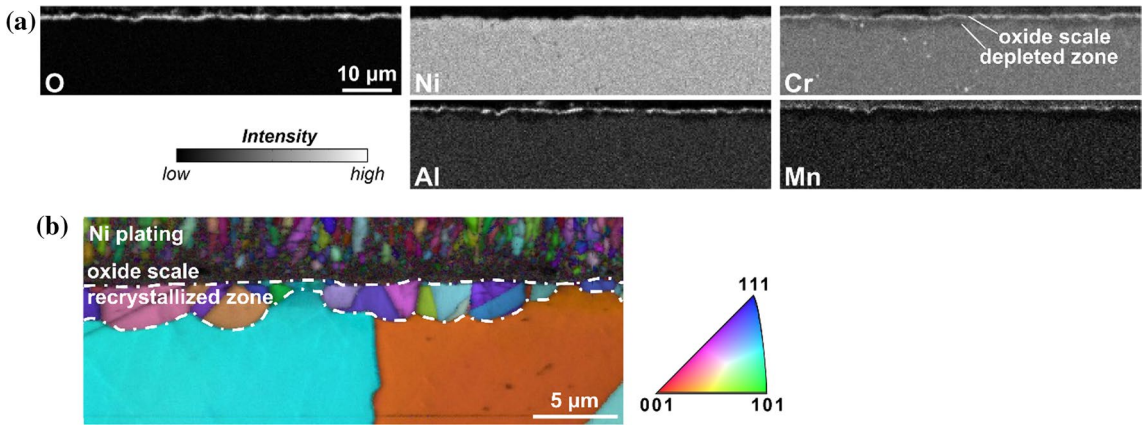

Figure 3 Cross sections of alloy 601 surface regions after exposure in gas II at 620 °C and 18 bar for 960 h. **a** element maps (EPMA) of O, Ni, Cr, Al, and Mn. **b** Color coded EBSD map (FCC). The image quality is overlayed, with darker regions representing a lower image quality. Adapted from [28]

oxide (not shown for clarity). Si was enriched close to the surface after exposure in gas I and IV (also not shown for clarity). The maximum Al content of the scale grown in gas IV was lower than in the other gases. This gas IV sample was exposed for only 480 h (compared to nearly 1000 h for the others), so the lower Al content can be attributed to the slow diffusion of Al at the test temperature. Significant C enrichment, with a maximum at the gas/oxide interface, was noted for the samples exposed in gases III and IV. Grabke et al. [29] reported a similar carbon profile in the oxide scale formed on an AISI 304 steel after exposure to a CO–H_2–H_2O mixture at 650 °C.

Raman spectroscopy was used to identify the phases present in the complex oxide scales. The averaged spectra for each gas exposure are compared in Fig. 6.

The bands at 300, 350, 560 and 620 cm^{-1} were attributed to chromia [30] and the bands at 690 cm^{-1} to Cr-Mn spinel [31]. However, identification of the weaker bands at 530 cm^{-1}, around 650 cm^{-1} and the shoulder around 710 cm^{-1} were not fully clear. They could all be attributed to MnO_2, with the shoulder around 710 cm^{-1} caused by $V_O^{\bullet\bullet}$ in MnO_2 [32]. Alternatively, the band at 530 cm^{-1} could be assigned to chromia [30] and the band around 650 cm^{-1} to a minor enrichment of chromia with Fe [33]. The shoulder at 710 cm^{-1} could also have indicated a partial substitution of Cr^{3+} (75,5 pm diameter [34]) in the octahedral positions of the Cr-Mn spinel by smaller cations [30, 32, 35], in this case most likely to be Al^{3+} (67,5 pm diameter [34]). However, this was ruled out using the TEM–EDX measurements (see below) which do not show Al in the outer

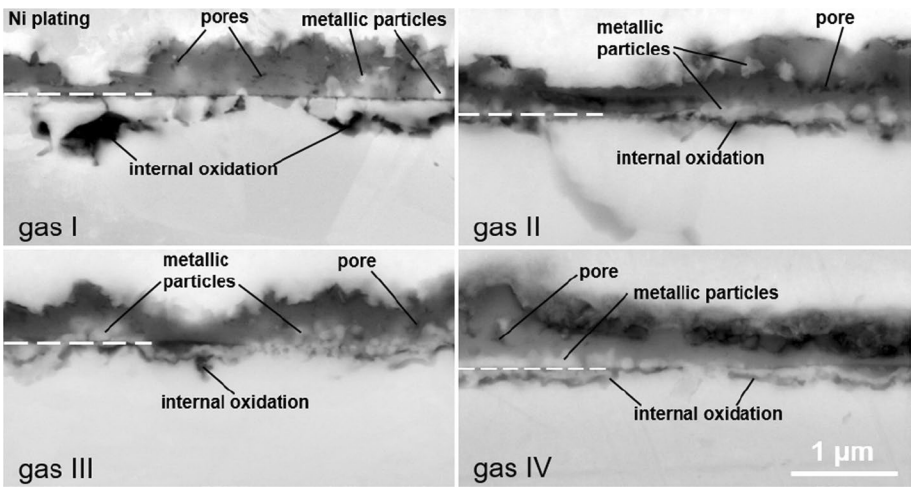

Figure 4 BSE images of 601 cross sections, samples exposed in gas I (960 h), gas II (960 h), gas III (980 h), and gas IV (480 h) at 620 °C and 18 bar. The dotted white lines indicate the location of the original sample surfaces. After [28]

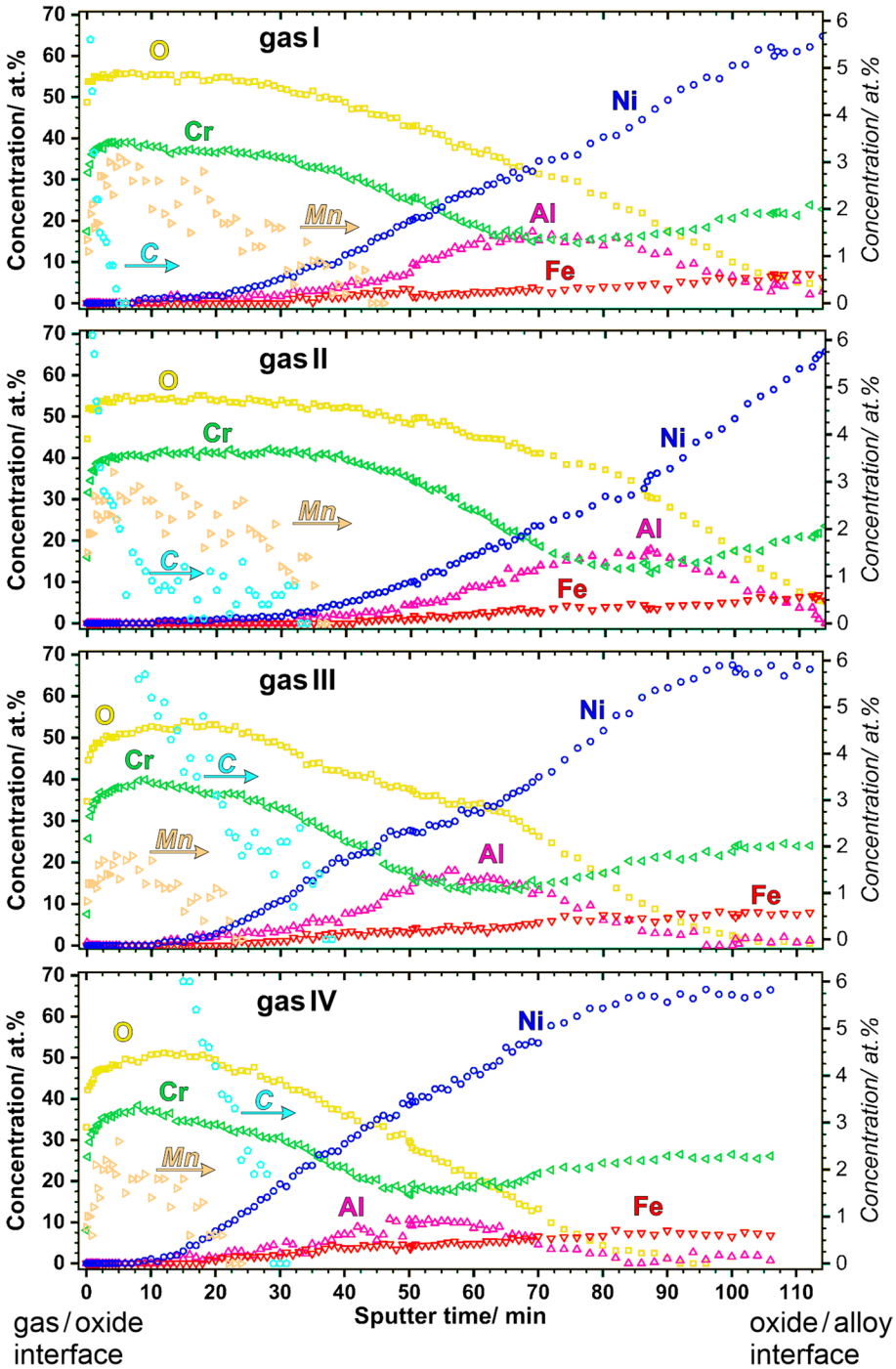

Figure 5 XPS depth profiles of alloy 601 samples after exposure in gas I (960 h), gas II (960 h), gas III (980 h), and gas IV (480 h) at 620 °C and 18 bar. The sputter time is indicative of the depth. Concentration of minor elements (C, Mn) are presented on the second y-axis. After [28]

Cr-Mn-spinel. No Si-oxides were detected with Raman spectroscopy. These would cause Raman bands at 460 cm^{-1} for amorphous SiO_2 [36], at 420 cm^{-1} for crystalline SiO_2 [37] and at 990 cm^{-1} for Cr-containing SiO_2 [38].

Some bands were omitted from Fig. 6 for clarity: locally appearing bands of TiO_2 (450 cm^{-1} and 610 cm^{-1} [39]); weak, local bands of γ-, θ- and α-Al_2O_3 (increase around 1100 cm^{-1}; bands at 1170 cm^{-1}; bands at 1390 cm^{-1} and 1410 cm^{-1}, respectively [40, 41]) and on all samples the C- and G-bands of carbon (1350 and 1600 cm^{-1} [42, 43]). In total, no shift of the bands or differences in the bands' intensity ratios were observed when comparing the samples exposed in the different

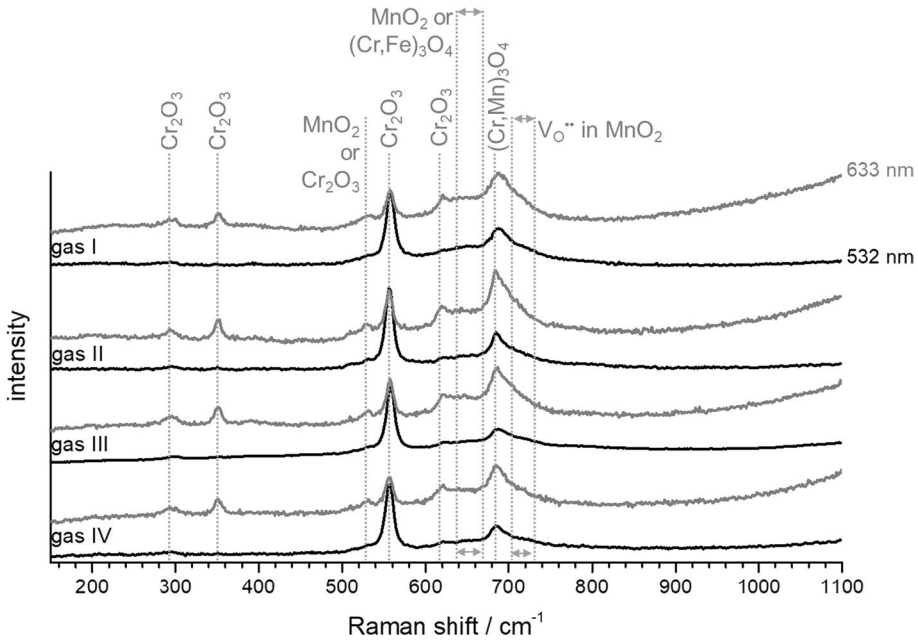

Figure 6 Raman spectra of the surfaces of alloy 601 after exposure in gas I (960 h), gas II (960 h), gas III (980 h), and gas IV (480 h) at 620 °C and 18 bar. Each spectrum is an average of at least five measurements. Lasers with 532 and 633 nm wavelengths were used. After [28]

gases. Hence, the compositions of the oxides were independent from the gas composition.

For a more detailed understanding of the microstructural features within the complex oxide scales, representative regions were prepared for further TEM investigations. Samples from gases II and IV were selected for the TEM investigations, as the former showed the earliest pit formation, while the latter showed strong attack overall (Fig. 1). Figure 7 gives HAADF micrographs of the oxide scales and TEM–EDX concentration profiles along the indicated lines.

No structural differences were apparent between the alloy 601 oxide scales after exposure in gas II and IV. The elemental distributions were mostly comparable. The EDX analyses showed that besides O, the outward grown scales contained predominantly Cr and some Mn. The Mn-rich parts contained 60 at.% O, 24 at.% Cr, and 12 at.% Mn (Fig. 7d), which is close to the expected composition of $MnCr_2O_4$. The BSE micrographs indicated the formation of internal oxide phases (dark-appearing) that formed locally. The concentration profile in Fig. 7d confirmed that these internal oxides were rich in Al. On top of the Al_2O_3 layer, Si enrichment was measured. The surface regions where the internal oxides did not form (Fig. 7c) indicated the same progression of a thin Si-rich oxide above the Al-rich layer. In these areas, the initially formed Al was still protective and considerably thinner. No depletion of Cr below 15 at.% was observed in the first hundred nanometers below the oxide scale after 960 h of exposure in gas II and after 480 h in gas IV. Additionally, the metallic particles (as described in Fig. 4) can be seen in both the gas II and gas IV outer oxide scales. The EDX measurements indicated primarily Ni enrichment and to a lower extent Fe within these particles. Less than 0.5 at.% Al and Si were detected within the individual particles.

The distribution of C in the oxide scale was also of interest to investigate with STEM-EDX and therefore a second lamella of the oxide scale after exposure to gas IV was prepared and analyzed. Figure 8 shows an overview of the region of interest along with high-resolution micrographs from selected areas. To provide further evidence of the highly localized enrichment of C, the elemental distribution maps from the displayed region (Fig. 8a) are shown separately in Fig. 9. Additional elemental distribution maps from the displayed sample regions in Fig. 7 are summarized in Online Resource 1.

A considerable degree of porosity is evident in the outer oxide layers. Interestingly, both C ingress and metal particles, which exhibit a large distance from the original alloy surface, coincide with these pores. The microstructure of the C-containing oxide and an adjacent region were investigated with higher detail in Fig. 8c, d. Figure 8c indicates lattice fringes that appear curved. In smaller partitions, these fringes

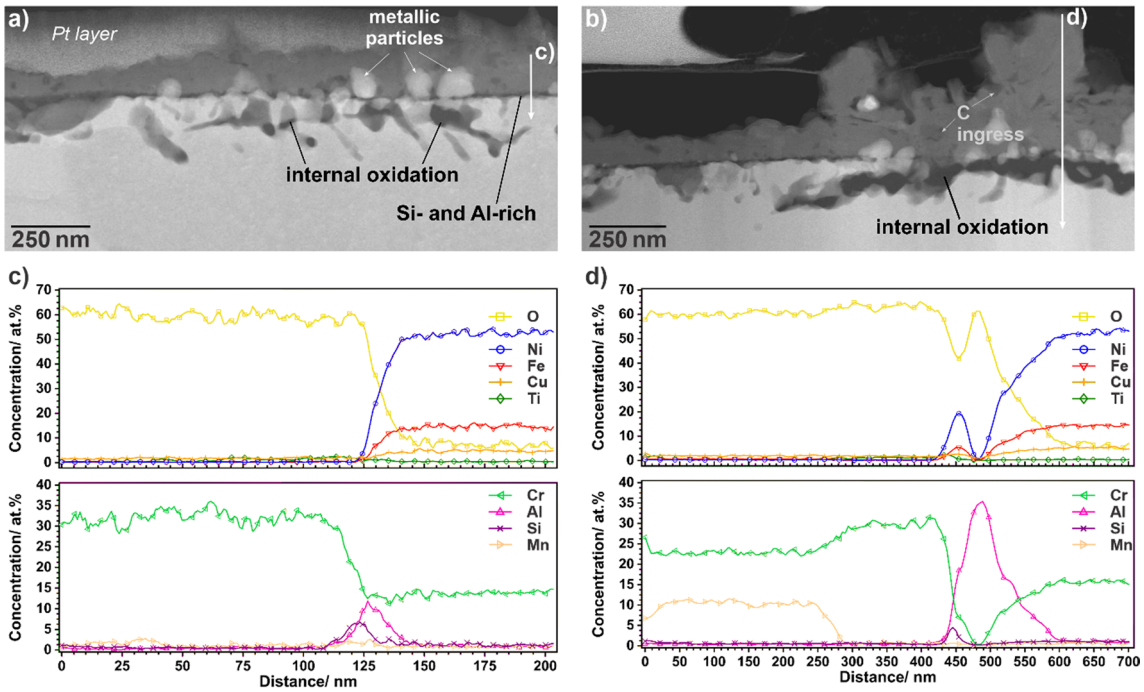

Figure 7 STEM HAADF micrographs of representative oxide scale regions in alloy 601 after exposure for 960 h in gas II (**a**) and 480 h in gas IV (**b**) at 620 °C and 18 bar. The displayed elemental profiles (c,d) were extracted from elemental distribution maps. Stronger oxide forming elements were plotted separately

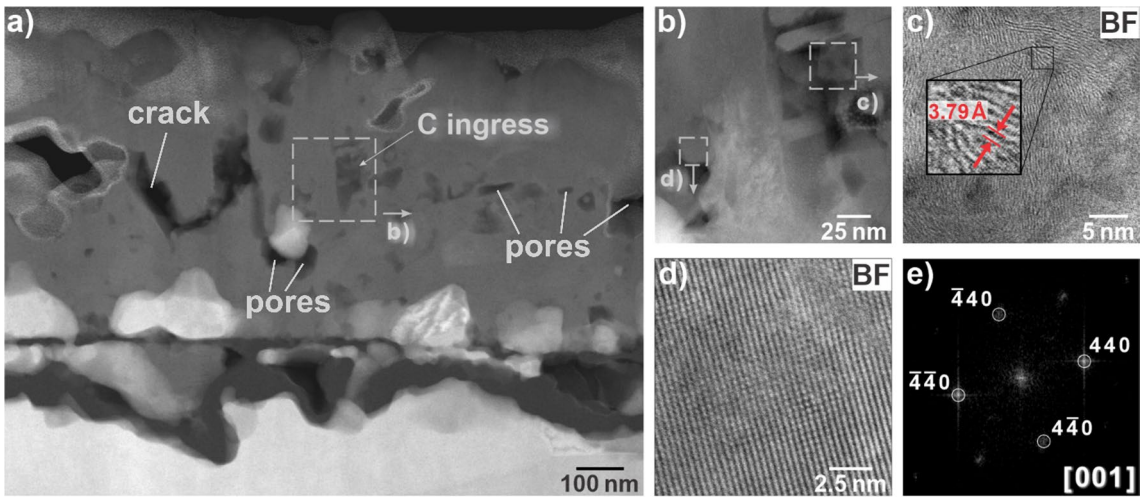

Figure 8 STEM micrographs of the oxide scale of alloy 601 after exposure for 480 h in gas IV at 620 °C and 18 bar. **a** Overview with C ingress labeled. **b–d** Detailed views of individual sections. **e** Fast Fourier transform (FFT) of the bright field (BF) atomically resolved micrograph in **d** with the Cr_2O_3 lattice reflections (with the [0 0 1] zone axis) labeled

are, to a certain degree, parallel. At higher magnifications, the distance between the individual fringes (shown as an insert) was determined to be 3.79 Å. This spacing is in good accordance with the distance between graphite (002) planes [44, 45]. A fast Fourier transform (FFT) of the bright field (BF) image of the region in Fig. 8d with atomic resolution was calculated and compared with literature databases. The lattice reflections corresponded to M_2O_3 structures, such as Cr_2O_3.

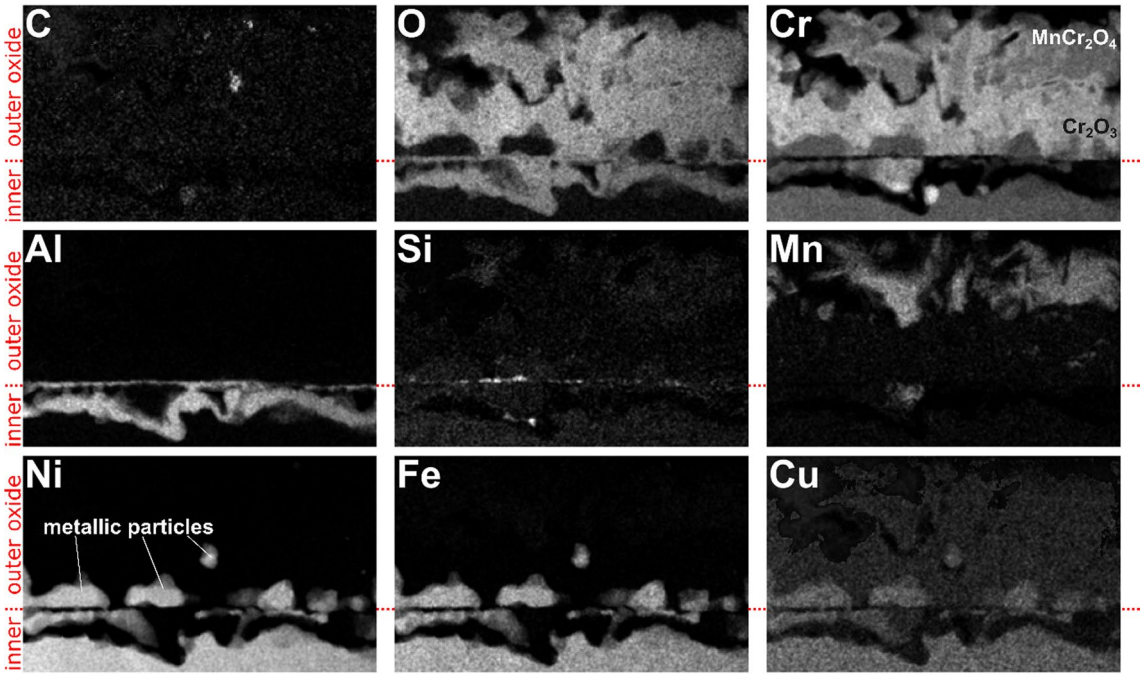

Figure 9 Elemental distribution maps in the surface region of alloy 601 after exposure for 480 h in gas IV at 620 °C and 18 bar (compare to HAADF STEM micrograph in Fig. 8a). The dotted red lines next to the images indicate the location of the original surface

STEM-EDX maps indicating the distribution of the relevant elements are summarized in Fig. 9.

Only highly localized C was observed in the outer oxide layer. The significant C signal in the elemental distribution maps must originate from the graphite-like structure within the oxide scale. The distribution of Cr indicated that the outer oxide layer could be separated into two parts. The first only contains signal from O and Cr and the second also includes a considerable contribution from Mn. Together with the FFT information (Fig. 8e), Cr_2O_3 can be confirmed as the dominant oxide phase closer to the original alloy surface. As described above, the Mn-containing oxide was identified as the $MnCr_2O_4$ spinel phase. In the image of the displayed oxide scale, on the left side Cr_2O_3 and $MnCr_2O_4$ are clearly separated by a crack (see also Fig. 8a). In the right region, the demarcation line between the two phases also appears to contain a higher density of small pores.

A thin Al-rich layer developed directly below the outer oxide layer; however, it is likely not continuous due to the large amount of internal Al oxidation. As described above, Si was adjacent to the thin Al-containing oxide layer at the original sample interface. The intensity of Si was even less homogeneously distributed in this region. Supporting the results from the elemental profiles (Fig. 7 c,d), Ni, Fe, and Cu were not present in the oxide. Ni and Fe were present as the main content of the metallic particles. The signal of Cu was significantly lower and appeared in coinciding regions with Ni and Fe. The Ti map was not included since no significant intensities were measured.

The presence of the metallic particles in the outer oxide scale were important to characterize in further detail to determine their influence on the resistance of the scale against carbon ingress and metal dusting attack. For a more detailed understanding, the compositions of 15 metallic particles were analyzed from TEM lamellae (one from the sample exposed in gas II and two from the samples exposed in gas IV). The average compositions versus the distance of the center of the particle to the SiO_x-layer, as an indication for the initial metallic surface, are shown in Fig. 10.

The metallic particles contain less than 0.5 at.% Al, which is significantly less than the alloy (2.5 at.%). Particles further away from the initial metal surface show lower Cr content, while Ni is correspondingly enriched. Fe is also generally enriched in the particles.

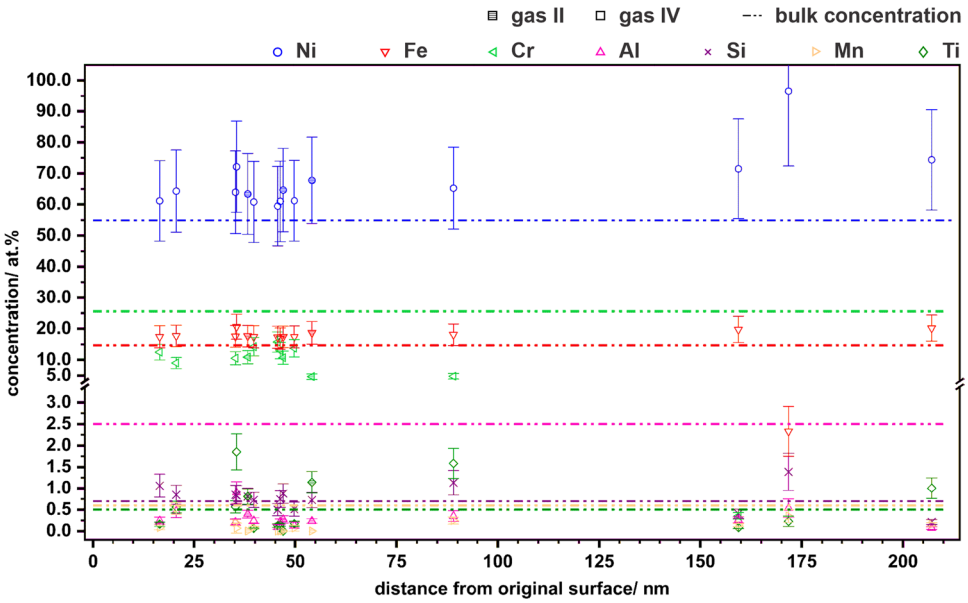

Figure 10 Compositions of the metallic particles in the oxide scale versus their distance to the SiO_X- layer, on samples of alloy 601 after exposure for 960 h in gas II (filled symbols) and for 480 h gas IV (open symbols) at 620 °C and 18 bar. Dotted lines indicate the bulk composition of the alloy, as given in Table 1

Discussion

In this study, the oxide scale formation during metal dusting of alloy 601 was studied in four different gas compositions. The differences in the gas compositions, and thereby the change in driving force for carbon deposition, and the performance of other commercial alloys in these conditions has been described elsewhere [21]. No attack was observed in gas I, while the aggressivity of the attack increased from gas II to gas IV (Fig. 1). The aim of the present study was to evaluate if and how the microstructure of the oxide scale depends on the gas composition, and thus how failure of the oxide scale occurs, allowing C ingress and eventual pit formation.

The proposed schematic model of the microstructure of the oxide scale is shown in Fig. 11, and the connected failure mechanisms are outlined in the following.

In contrast to the typically rougher surfaces in application, the samples were all ground to P1200 grit (SiC paper) to reduce the impact of surface roughness and deformation. This simplifies the study of the more fundamental mechanisms in the oxide scale formation and failure. In both laboratory and industrial applications, a native oxide scale forms in ambient conditions

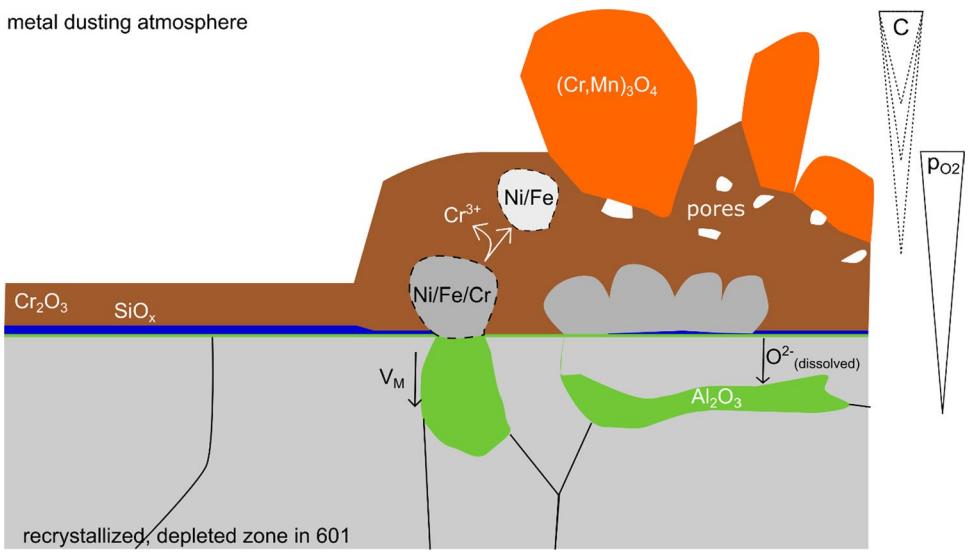

Figure 11 Schematic model of the oxide scale formed on alloy 601 after exposure under metal dusting conditions at 620 °C and 18 bar. The main difference in microstructure of the oxide scales formed in gas I to IV is the amount and depth of the carbon enrichment. Adapted from [28]

before exposure to gases at high temperatures. After exposure, the metallic matrix below the oxide was recrystallized (Fig. 3), most probably caused by the residual stresses due to surface preparation prior to exposure. The dislocations induced by grinding can initiate recrystallization at 620 °C [46]. Another contribution can come from the depletion of the oxide formers, leading to nanoscale residual stresses (Fig. 3). At these temperatures, diffusion through the bulk crystal lattice is relatively slow and the oxide formers mainly diffuse along short-circuit paths [47, 48].

On the left side of the schematic is an example of the protected areas where below the outward growing chromia layer, Si was enriched (TEM–EDX maps in Fig. 9). It is well known from similar materials that Si-rich oxides form at the oxide/metal interface and reduce the outward diffusion of Cr^{3+} [49–53]. The Si-rich phase (dark contrast) was more pronounced in areas with a thin chromia layer (BSE images in Fig. 4 and (S)TEM HAADF micrographs in Fig. 7). This thin duplex scale is an indication that the formed scale was protective in these regions. In the Raman spectra, neither amorphous nor crystalline silica was detected. As the thermodynamic stability of silica is between that of alumina and chromia (Table 3), the Si-rich regions are most likely silica despite the lack of definitive information from Raman and XPS.

On the right side of the schematic in Fig. 11, the second type of microstructure is outlined. Here, the Si oxide layer is thinner and discontinuous, while the outer chromia scale is significantly thicker. Grains of Cr-Mn spinel formed in the outer scale, as demonstrated by the XPS depth profiles (Fig. 5), the Raman band at 690 cm^{-1} (Fig. 6), and the TEM–EDX element maps (Fig. 9). The formation of Cr-Mn spinels on top of chromia is often observed on commercial alloys even though $MnCr_2O_4$ is stable at lower p_{O2} than chromia at 620 °C (Table 3). This effect is accounted for by the low Mn concentration in the alloy, the low Mn activity in the oxide [57, 58] as well as its fast diffusion within the oxide scale.

The chromia/spinel ratio of the oxide scales was consistent for all four tested gas mixtures (Raman spectroscopy, Fig. 6). Contrary to this, Guo et al. [8] showed an increased formation of chromia on 601 at 750 °C in 10 vol.% CO, 90% Ar compared to 20% CO, 25% H_2, 15% CO_2, 10% H_2O and 30% Ar. Thus, the formation of spinel might be favored over chromia by the presence of CO_2, H_2O and H_2, which were all components of the gas mixtures used in the current study.

Generally, the formation of a continuous, dense alumina layer provides excellent protection against metal dusting attack [59]. However, Fabas et al. [60] reported a higher resistance of alloy 690, with no nominal Al content, than alloy 693 with 3 wt.% Al in a metal dusting environment at 570 °C. They held the absence of alumina formation on 690 responsible for the better performance. Similarly, Rouaix Vande-Put et al. [61] argued that the failure of the chromia scale on 601 could be ascribed to internal oxidation of Al.

Additionally, internal oxidation may result in the formation of metallic particles in the oxide scale. Two mechanisms have been proposed in the literature: (1) The volume increase during internal oxidation causes compressive stresses on the metal matrix and (2) outward diffusion of the metal ions occurs due to activity gradients. For the first mechanism, the compressive stresses can be partly released by vacancy diffusion in the metal [62, 63]. This is analogous to Nabarro-Herring creep [63]. In the presence of phase or grain boundaries (from recrystallization or internal oxidation), vacancy diffusion is faster along these paths (Coble creep [63, 64]). As a result of metal vacancy diffusion, metallic particles form in the oxide scale. Interestingly, simultaneous tensile stresses are expected beneath the oxide scale from Cr, Si, and Mn outward diffusion. The zone depleted in these elements is deeper (1–3 µm) than the internal oxidation (around 0.2 µm). Hence, both stress types may coexist in the different layers of the metal. For the second mechanism Schimmel et al. [65] proposed diffusion based on the activity gradients of the unoxidized metallic elements. The metal cations diffuse outwards according to the activity gradient and thus metallic particles

Table 3 Calculated p_{O2} of oxide dissociation [54–56] and gas compositions at thermodynamic equilibrium [26], all at 620 °C, ordered by decreasing p_{O2}

Oxides	p_{O2}	Gases
Fe_2O_3	3.3×10^{-15}	
NiO	2.5×10^{-19}	
	7.5×10^{-23}	IV
	1.8×10^{-23}	III
	4.0×10^{-24}	II
Fe_3O_4	3.5×10^{-24}	
	8.6×10^{-25}	I
FeO	7.0×10^{-25}	
Cr_2O_3	2.0×10^{-35}	
$MnCr_2O_4$	2.1×10^{-38}	
SiO_2	2.0×10^{-44}	
Al_2O_3	1.5×10^{-53}	

outside of the initial metal surface are formed. In the investigated oxide scales, most of the metallic particles in the outer scale accumulated next to the original sample surface, but a few particles were at a greater distance within the oxide scale. TEM–EDX of the further outward particles showed that they contained less Cr than the particles located close to the oxide/metal interface (Fig. 10). As the oxygen activity increases toward the gas/oxide interface, Cr is oxidized, and particles enriched in Ni and Fe remain.

According to the thermodynamic stability of the oxides (Table 3), formation of FeO for all gas compositions and formation of Fe_3O_4 for gases II, II and IV should be possible. However, only one of the metallic particles further from the original alloy surface was depleted in Fe, indicating the oxidation of Fe. Thus, no definite conclusions can be drawn about the oxidation of Fe from the limited number of studied particles.

The microstructure of the oxide scale elucidates the failure mechanisms. In comparison with the mechanisms proposed in literature, the failure cause is not due to a single reason, but is instead the collective effect of several mechanisms:

Cracks: gas transport through the oxide In the analyzed samples, no cracks were observed (yet). However, the outer oxide contained significant porosity. Gas ingress and subsequent carbon deposition on the alloy is possible if open porosity is connected throughout the entire scale. In that case, simultaneous oxidation would also be expected. Even though the alloy at the oxide/metal interface is slightly depleted in Cr, formation of a chromia scale would still be possible from the remaining Cr content of 15–19 at.%. Hence, further carbon ingress should be hindered at the oxide/metal interface unless additional depletion occurs after very long exposure times.

Spinels: enhanced CO dissociation and/or carbon diffusion The local formation of Mn-Cr spinel in the oxide scale has been confirmed for alloy 601. A higher carbon solubility has been attributed for this spinel than for chromia [9] and thus this spinel formation supports carbon transport through the scale.

Metallic Ni-rich particles: enhanced carbon diffusion The presence of metallic particles in the oxide scale has also been confirmed. Zeng et al. [16] proposed that the metallic particles formed by the reduction of Ni- and Fe-rich spinels, however, this was not observed in these environments for alloy 601. A new mechanism is instead proposed: internal oxidation of aluminum drives metallic particles into the oxide scale through compressive stresses and/or activity gradients. The particles initially maintain a similar composition as the metallic matrix, but during outward transport of the particles to higher oxygen activities, Cr is oxidized. As a result, Ni-rich metallic particles remain.

Carbon enrichment along (oxide) grain boundaries: enhanced carbon diffusion It is important to note that the metallic particles mentioned here and formed in the oxide scale have a different origin and role during metal dusting failure than the metal nano-particles present in the coke which forms after pit initiation [66].

The XPS depth profiles and Raman spectra showed carbon enrichment in the oxide scales. Even though carbon is present in the oxide, no complete and fast diffusion paths through the scale were directly observed, as no pits initiated in the analyzed regions. Regions that were locally enriched with carbon suggest it is present as graphite within Cr_2O_3 (Fig. 8). This 'graphitization' of chromia might be an indication of the later stage of metal dusting attack reached in gas IV. The dissolution of C in the oxide scale cannot be confirmed nor excluded from the results of the present study. However, some indication can be inferred from the more significant carbon accumulation in the oxide scales formed in the more aggressive gases III and IV (Fig. 5).

In total, the combined interaction between interconnected porosity, metallic particles in the oxide, enhanced carbon solubility in Cr-Mn spinels, and carbon enrichment in the scale is proposed as the mechanism for failure of the oxide scale. Carbon can access the Ni-rich particles close to the gas/oxide-surface via pores, cracks, oxide grain boundaries or a spinel phase. Then, carbon can dissolve in the metal, supersaturate and graphite formation can occur [43, 66]. Volume expansion from the graphite formation then spalls off the oxide scale above the metallic particles. In the unfortunate case where several metallic particles, spinel grains, C-rich grain boundaries and/or pores are adjacent to each other, they can form a path for carbon deeper into the scale and even potentially to the metal substrate. In this way, pit formation can be initiated.

The amounts of spinel formation, metallic particles and porosity were apparently unaltered in the varying gas compositions. These factors are clearly more determined by the alloy composition and sample properties, such as the surface deformation, which contribute to diffusion and thus the oxide scale microstructure.

Separately, the temperature, which also contributes to the elemental diffusion rates, was not varied in this particular study, but would have an influence on the resulting oxide scale.

The last factor of the combined failure mechanism, carbon enrichment, changes with the driving force of the gas for carbon deposition. While there was some indication of variation in the carbon deposition profiles as a function of the gas aggressivity, this is worthy of further study in order to better clarify the degree of influence the various factors have in the combined mechanism.

This mechanism for the oxide scale failure also specifically confirms the fairly well established methods for metal dusting attack mitigation. To minimize the oxide scale failure followed by metal dusting pit initiation, and thus metal dusting attack, the variables of the gas composition (driving force for carbon deposition) and/or the alloy composition and part preparation (oxide scale formation with minimal defects) can be adjusted and optimized.

Conclusion

The oxide scale microstructure and mechanism of failure of alloy 601 under exposure in different metal dusting gases was studied. A combination of four microstructural features of the oxide scale form a combined failure mechanism based on the high-resolution and detailed characterization.

Three of the four features are determined by the alloy composition and part preparation:

- Cracks: gas transport through the oxide
- Spinels: enhanced CO dissociation and/or carbon diffusion
- Metallic Ni-rich particles: enhanced carbon diffusion

Only one of the microstructural features is strongly influenced by the gas composition:

- Carbon enrichment along (oxide) grain boundaries: enhanced carbon diffusion

This combined failure mechanism gives a more complete picture of the means for carbon penetration of the oxide scale in a metal dusting environment and therefore metal dusting pit initiation. With this, the established methods for metal dusting attack mitigation are confirmed (reducing the driving force for carbon deposition by modifying the gas composition, choosing a higher alloyed material or optimizing the part preparation).

Acknowledgements

The authors are grateful for the assistance of Maciej Bik for Raman interpretation, Mathias Röhrig for experiments, Gerald Schmidt for EPMA, Melanie Thalheimer for EBSD and SEM, Susann Rudolphi for metallographic cross section preparation, and Silvia Ulrich for comments and discussions on the developed model. Martin Weiser is grateful for support by the Competence Center Engineering of Advanced Materials (FAU EAM). Support by CENEM through Dr. Yokosawa and Prof Spiecker during TEM data acquisition and interpretation is highly acknowledged. This work was supported by German Federal Ministry for Economic Affairs and Climate Action via IGF number 20854 N. Martin Weiser and Peter Felfer acknowledge the financial support from the European Research Council under the European Union's Horizon 2020 research and innovation programme under grant agreement No 805065. Emma White and Clara Schlereth have received funding from the European Union's Horizon 2020 research and innovation programme under grant agreement No 958192.

Funding

Open Access funding enabled and organized by Projekt DEAL.

Supplementary Information The online version contains supplementary material available at https://doi.org/10.1007/s10853-023-09260-2.

References

[1] Young DJ, Zhang J, Geers C, Schütze M (2011) Recent advances in understanding metal dusting: a review. Mater Corros. https://doi.org/10.1002/maco.201005675

[2] Grabke HJ (2003) Metal dusting. Mater Corros 54(10):736–746

[3] Baker RTK, Barber MA, Harris PS, Feates FS, Waite RJ (1972) Nucleation and growth of carbon deposits from the nickel catalyzed decomposition of acetylene. J Catal 26:51–62

[4] Zhang J, Cole DMI, Young DJ (2004) In: Proceedings of the EFC Workshop

[5] Zhang J, Munroe PR, Young DJ (2008) Microprocesses in nickel accompanying metal dusting. Acta Mater 56:68–77

[6] Zeng Z, Natesan K (2006) Initiation of metal-dusting pits and a method to mitigate metal-dusting corrosion. Oxid Met 66(1/2):1–20

[7] Nishiyama Y, Otsuka N, Kudo T (2006) Metal dusting behaviour of Cr–Ni steels and Ni-base alloys in a simulated syngas mixture. Corros Sci. https://doi.org/10.1016/j.corsci.2005.08.008

[8] Guo X, Vanhaecke E, Vullum PE, Ma J, Gunawardana PDS, Walmsley JC, de Chen VHJ (2020) Effects of metal dusting relevant exposures of alloy 601 surfaces on carbon formation and oxide development. Catal Today. https://doi.org/10.1016/j.cattod.2020.04.029

[9] Galetz MC, Schlereth C, White EMH, Boll T, Bik M, Sitarz M, Chen W-T, Gleeson B (2023) An expanded model for the pressure effect in metal dusting of Mn-containing alloy 600 based on advanced scale characterization. High Temp Corros Mater. https://doi.org/10.1007/s11085-023-10201-2

[10] Kato H, Kodoma T, Tsuji M, Tamaura Y, Chang SG (1994) Decomposition of carbon dioxide to carbon by hydrogen-reduced Ni(II)-bearing ferrite. J Mater Sci 29(21):5689–5692. https://doi.org/10.1007/BF00349965

[11] Tabata M, Akanuma K, Nishizawa K, Mimori K, Yoshida T, Tsuji M, Tamaura Y (1993) Reactivity of oxygen-deficient Mn(II)-bearing ferrites ($MnxFe_{3-x}O_{4-d}$, O<x<1, d>0) toward CO_2 decomposition to carbon. J Mater Sci 28(24):6753–6760. https://doi.org/10.1007/BF00356427

[12] Hwang C-S, Wang N-C (2004) Preparation and characteristics of ferrite catalysts for reduction of CO_2. Mater Chem Phys. https://doi.org/10.1016/j.matchemphys.2004.02.028

[13] Zeng Z, Natesan K, Grimsditch M (2004) Effect of oxide scale compositions on metal dusting corrosion of Fe-based alloys. Corr 60(7):632–642

[14] Li H, Chen W (2011) High temperature carburization behaviour of Mn–Cr–O spinel oxides with varied concentrations of manganese. Corros Sci. https://doi.org/10.1016/j.corsci.2011.02.021

[15] Li H, Zheng Y, Benum LW, Oballa M, Chen W (2009) Carburization behaviour of Mn-Cr-O spinel in high temperature hydrocarbon cracking environment. Corros Sci. https://doi.org/10.1016/j.corsci.2009.06.006

[16] Zeng Z, Natesan K, Cai Z, Darling SB (2008) The role of metal nanoparticles and nanonetworks in alloy degradation. Nat Mater. https://doi.org/10.1038/nmat2227

[17] Christ H-J, Künecke U, Meyer K, Sockel HG (1988) Mechanisms of high-temperature corrosion in helium containing small amounts of impurities II corrosion of the nickel-base alloy inconel 617. Oxid Met 30(1):27–51

[18] Nguyen TD, La Fontaine A, Yang L, Cairney JM, Zhang J, Young DJ (2018) Atom probe study of impurity segregation at grain boundaries in chromia scales grown in CO_2 gas. Corros Sci. https://doi.org/10.1016/j.corsci.2017.12.024

[19] Li B, Gleeson B, Chen W-T, Hattendorf H (2020) In: Proceedings of Corrosion 2020. NACE

[20] Röhnert D, Phillipp F, Reuther H, Weber T, Wessel E, Schütze M (2007) Initial stages in the metal-dusting process on alloy 800. Oxid Met. https://doi.org/10.1007/s11085-007-9075-9

[21] Schlereth C, Hack K, Galetz MC (2022) Parameters to estimate the metal dusting attack in different gases. Corros Sci. https://doi.org/10.1016/j.corsci.2022.110483

[22] Grabke HJ, Müller-Lorenz EM, Strauss S, Pippel E, Woltersdorf J (1998) Effects of grain size, cold working, and surface finish on the metal-dusting resistance of steels. Oxid Met 50(3/4):241–254

[23] White E, Schlereth C, Lepple M, Hattendorf H, Nowak B, Galetz MC (2022) Influence of surface treatment on the metal dusting behavior of alloy 699 XA. Mater Corros. https://doi.org/10.1002/maco.202213380

[24] Schlereth C, White EMH, Lepple M, Nowak B, Hattendorf H, Galetz MC (2023) Influence of surface treatment on metal dusting resistance of welds. Mater Corros. https://doi.org/10.1002/maco.202313954

[25] Madloch S, Soleimani-Dorcheh A, Galetz MC (2018) Effect of Pressure on Metal Dusting Initiation on Alloy 800H and Alloy 600 in CO-rich Syngas. Oxid Met 89(3–4):483–498
[26] Bale CW, Bélisle E, Chartrand P, Decterov SA, Eriksson G, Gheribi AE, Hack K, Jung I-H, Kang Y-B, Melançon J, Pelton AD, Petersen S, Robelin C, Sangster J, Spencer P, van Ende M-A (2016) FactSage thermochemical software and databases, 2010–2016. Calphad. https://doi.org/10.1016/j.calphad.2016.05.002
[27] Menges F (2020) Spectragryph - optical spectroscopy software
[28] Schlereth C (2023) Umgebungseinfluss auf die Oxidschichtbildung in befeuchteter Luft und bei Metal Dusting-Bedingungen
[29] Grabke HJ, Müller-Lorenz EM (1998) Protection of high alloy steels against metal dusting by oxide scales. Mater Corros 49:317–320
[30] Hosterman BD (2011) Raman spectroscopic study of solid solution spinel oxides
[31] Chen Y, Liu Z, Ringer SP, Tong Z, Cui X, Chen Y (2007) Selective oxidation synthesis of $MnCr_2O_4$ spinel nanowires from commercial stainless steel foil. Cryst Growth Des. https://doi.org/10.1021/cg070514a
[32] Bik M, Galetz M, Dąbrowa J, Mroczka K, Zając P, Gil A, Jeleń P, Gawęda M, Owińska M, Stygar M, Zajusz M, Wyrwa J, Sitarz M (2022) Polymer derived ceramics based on SiAlOC glasses as novel protective coatings for ferritic steel. Appl Surf Sci. https://doi.org/10.1016/j.apsusc.2021.151826
[33] McCarty KF, Boehme DR (1989) A raman study of the systems $Fe_{3-x}Cr_xO_4$ and $Fe_{2-x}Cr_xO_3$. J Solid State Chem 79:19–27
[34] Holleman AF, Wiberg E, Wiberg N, Eagleson M, Brewer W, Aylett BJ (2001) Inorganic chemistry, 1st edn. Academy Press, San Diego
[35] Madern N, Monnier J, Baddour-Hadjean R, Steckmeyer A, Joubert J-M (2018) Characterization of refractory steel oxidation at high temperature. Corros Sci. https://doi.org/10.1016/j.corsci.2017.12.029
[36] Bates JB, Quist AS (1972) Polarized Raman Spectra of β-Quartz. J Chem Phys. https://doi.org/10.1063/1.1677402
[37] Bates JB (1972) Raman spectra of α and β cristobalite. J Chem Phys. https://doi.org/10.1063/1.1678878
[38] Dines TJ, Inglis S (2003) Raman spectroscopic study of supported chromium(vi) oxide catalysts. Phys Chem Chem Phys. https://doi.org/10.1039/b211857b
[39] Hsu LS, Rujkorakarn R, Sites JR, She CY (1986) Thermally induced crystallization of amorphous-titania films. J Appl Phys. https://doi.org/10.1063/1.336817
[40] Tolpygo VK, Clarke DR (2000) In: Tatlock G, Newcomb SB (eds) Proceedings of the fourth international conference on the microscopy of oxidation, Trinity Hall, Cambridge, 20–22 September 1999, pp 59–70
[41] Grégoire B (2017) Functionalization of aeronautical thermal barrier systems elaborated by slurry (FONBAT)
[42] Tuinstra F, Koenig JL (1970) Raman spectrum of graphite. J Chem Phys. https://doi.org/10.1063/1.1674108
[43] Zeng Z, Natesan K (2003) Relationship of carbon crystallization to the metal-dusting mechanism of nickel. Chem Mater 15:872–878
[44] Chun CM, Bhargava G, Ramanarayanan TA (2007) Metal dusting corrosion of nickel-based alloys. J Electrochem Soc. https://doi.org/10.1149/1.2710215
[45] Chun CM, Ramanarayanan TA (2004) Metal-dusting corrosion of low-chromium steels. Oxid Met 62(1/2):71–92
[46] Zhang J, Young DJ (2007) Kinetics and mechanisms of nickel metal dusting I. Kinetics and morphology. Corros Sci 49:1496–1512
[47] Gheno T, Desgranges C, Martinelli L (2020) On the role of surface deformation in the oxidation of NiCr alloys at 340–600 °C. Corros Sci. https://doi.org/10.1016/j.corsci.2020.108805
[48] Hughes AE, Atkinson A, Chadwick AT (1983) Short-circuit diffusion processes in oxidation films. MRS Online Proc Libr. https://doi.org/10.1557/PROC-24-27
[49] Evans HE, Hilton DA, Holm RA, Webster SJ (1983) Influence of silicon additions on the oxidation resistance of a stainless steel. Oxid Met. https://doi.org/10.1007/BF00656225
[50] Young DJ (1982) Oxidation behaviour of some modern heat-resistant cast steels. High Temp Technol 1:101–105
[51] Sand T, Edgren A, Geers C, Asokan V, Eklund J, Helander T, Svensson JE, Johansson LG (2021) Exploring the effect of silicon on the high temperature corrosion of lean FeCrAl alloys in humid air. Oxid Met. https://doi.org/10.1007/s11085-020-10019-2
[52] Solimani A, Nguyen T, Zhang J, Young DJ, Schütze M, Galetz MC (2020) Morphology of oxide scales formed on chromium-silicon alloys at high temperatures. Corros Sci. https://doi.org/10.1016/j.corsci.2020.109023
[53] Ulrich AS, Pfizenmaier P, Solimani A, Glatzel U, Galetz MC (2020) Improving the oxidation resistance of Cr-Si-based alloys by ternary alloying. Corros Sci. https://doi.org/10.1016/j.corsci.2019.108376
[54] Young DJ (ed) (2016) High temperature oxidation and corrosion of metals, 2nd edn. Elsevier, London
[55] Barin I (2008) Thermochemical data of pure substances. VCH Weinheim, New York

[56] Allison T (1996) JANAF Thermochemical Tables, NIST Standard Reference Database 13. National Institute of Standards and Technology

[57] Stott FH, Wei FI, Enahoro CA (1989) The influence of manganese on the high-temperature oxidation of iron-chromium alloys. J Mater Eng Perform 40(4):198

[58] Talic B, Molin S, Hendriksen PV, Lein HL (2018) Effect of pre-oxidation on the oxidation resistance of Crofer 22 APU. Corros Sci. https://doi.org/10.1016/j.corsci.2018.04.016

[59] Hermse CGM, van Wortel H (2009) In: Proceedings of Corrosion 2009. NACE

[60] Fabas A, Rouaix-Vande Put A, Doublet S, Domergue D, Salem M, Monceau D (2017) Metal dusting corrosion of austenitic alloys at low and high pressure with the effects of Cr Al Nb and Cu. Corros Sci. https://doi.org/10.1016/j.corsci.2017.04.015

[61] Rouaix-Vande Put A, Unocic KA, Brady MP, Pint BA (2015) Performance of chromia- and alumina-forming Fe- and Ni-base alloys exposed to metal dusting environments: the effect of water vapor and temperature. Corros Sci 92:58–68

[62] Jiang C, Zhang J, Young DJ (2021) The effect of water vapor on NiO formation by Ni–Cr alloys at 650 °C (HTCPM Focus Issue, FNS-111). Oxid Met. https://doi.org/10.1007/s11085-021-10047-6

[63] Yi HC, Guan SW, Smeltzer WW, Petric A (1994) Internal oxidation of NiAl and NiAlSi alloys at the dissociation pressure of NiO. Acta Metall Mater. https://doi.org/10.1016/0956-7151(94)90292-5

[64] Coble RL (1963) A model for boundary diffusion controlled creep in polycrystalline materials. J Appl Phys. https://doi.org/10.1063/1.1702656

[65] Schimmel G, Sorina-Müller J, Kempf B, Rettenmayr M (2010) On the mechanism of Ag exudation during internal oxidation. Acta Mater. https://doi.org/10.1016/j.actamat.2009.11.051

[66] Park C, Rodriguez NM, Baker R (1997) Carbon deposition on iron-nickel during interaction with carbon monoxide-hydrogen mixtures. J Catal. https://doi.org/10.1006/jcat.1997.1691